THIRTEENTH EUROPEAN ROTORCRAFT FORUM

2.2

Paper No. 4

EULER SOLUTION OF MULTIBLADE ROTOR FLOW

C. L. Chen
Sterling Software, Palo Alto, California, U.S.A.

W. J. McCroskey
Aeroflightdynamics Directorate
U.S. Army Aviation Research and Technology Activity
Ames Research Center, Moffett Field, California, U.S.A.

S. X. Ying
Sterling Software, Palo Alto, California, U.S.A.

September 8-11, 1987

ARLES, FRANCE

ASSOCIATION AERONAUTIQUE ET ASTRONAUTIQUE DE FRANCE

EULER SOLUTION OF MULTIBLADE ROTOR FLOW

C. L. CHEN
Sterling Software, Palo Alto, California, U.S.A.

W. J. MCCROSKEY
Aeroflightdynamics Directorate
U.S. Army Aviation Research and Technology Activity
Ames Research Center, Moffett Field, California, U.S.A.

S. X. YING
Sterling Software, Palo Alto, California, U.S.A.

ABSTRACT

A numerical method for solving the Euler equations for multiblade rotors has been developed and some preliminary results are reported. The numerical scheme is a combination of several recent methods and algorithm improvements, adapted to the particular requirements of rotor-body interactions. A cylindrical basic grid has been used to study conventional multiblade helicopter rotors. Test calculations have been made for two- and six-blade rotors in hover and for a two-blade rotor in forward flight, under transonic tip conditions but without lift. The results show good agreement with experimental data.

1. INTRODUCTION

To date, computational work has involved a number of finite-difference or finite-volume schemes to simulate helicopter rotor flow by solving the potential, Euler or Reynolds-averaged Navier-Stokes equations. For most calculations, the computational domain covers only one blade arbitrarily and the rotor disk is computed only partially in the spanwise and circumferential direction. Therefore some physical boundary conditions are difficult to implement, and some artificial boundary conditions may be required. This work describes general grid topology which covers the entire rotor disk, or the partial rotor disk for the hovering case with physical periodic boundary conditions. The topology is also suitable for studying rotor-body interaction. Moreover, a new Euler solver for helicopter multiblade rotor flow is developed. The algorithm can be extended easily to solve the Reynolds-averaged Navier-Stokes equations . However, for a satisfactory viscous solution, a finer grid, high-order scheme and good turbulence model would be required. It would become too expensive to use in a routine production mode. In this paper, the grid topology, numerical algorithm, boundary-condition treatment, and verification are described. The computed results for nonlifting multiblade rotors in hover and in forward flight are compared with experimental data. The blade-to-blade aerodynamic interaction for nonlifting rotors is also studied.

2. GRID SYSTEM

Most grid topologies used for helicopter rotor flow until now were similar to those used for fixed-wing flow. That may be adequate for a one-blade rotor; however, those grid topologies are not appropriate or easily extended for multiblade

rotors. Indeed, it would seem quite difficult to generate a one-zone structure grid for the entire helicopter. The patched grid has been applied successfully in cascade (rotor-stator) flows by Rai.[1] In this paper, a similar cylindrical-type patched grid topology is proposed for the multiblade rotor and fuselage combination problem, which is shown in Fig. 1. The interpolation at the interface between the moving grid and the static grid is simplified by using this topology. A rotating C-type or O-type fine inner grid can be embedded to wrap the blade with a viscous zone. In the viscous zone, either Navier-Stokes or boundary layer equations would be solved.

The cylindrical rotating outer grid is generated by solving Poisson equations with periodic boundary conditions at blade cuts for a one-blade grid set. The periodic boundary conditions are $Z_1 = Z_{jmax}$ and $X_1 = X_{jmax} - \frac{2\pi r}{n}$. The r is the radius of each cylinder, X is the arc length along the circumferential direction and n is the number of blades. Therefore, a one-blade grid set can be rotated and connected to become a multiblade grid set. There are no discontinuities of grid slope between each blade grid. The grid set which is generated for a nonlifting four-blade rotor is shown in Fig. 2. In this paper, only the Euler calculation for the nonlifting rotors is included. The rotating outer grid provides enough resolution for the inviscid flow.

3. INTEGRAL FORMULATION

In this investigation, the finite-volume approach is adopted for three reasons: (a) it is more natural when considering conservation laws, (b) it can avoid metric singularities that are usually associated with finite-difference methods, and (c) it can capture free-stream conditions without numerical errors. The general form of a conservation law applied to an arbitrary grid cell is[2]

$$\int_{V(t_2)} U\,dV - \int_{V(t_1)} U\,dV + \int_{t_1}^{t_2} \oint_{S(t)} \mathbf{n}\cdot\mathbf{F}\,dS\,dt = 0 \tag{1}$$

where $V(t)$ is the cell volume, $\mathbf{n}\,dS(t)$ is a vector element of surface area with outward normal $\mathbf{n}$, U is a conservative variable per unit volume, and $\mathbf{F}$ is the flux of U per unit area per unit time. Let $\mathbf{u}$ and $\mathbf{v}(t)$ be the fluid velocity and cell-surface element velocity, respectively. The flux $\mathbf{F}$ can then be written as

$$\mathbf{F} = (\mathbf{u} - \mathbf{v})U + \mathbf{G} \tag{2}$$

where the first term is the convection of U relative to the surface element, and $\mathbf{G}$ stands for the non-convective part of the flux. Although Eq. (1) is general and rigorous, the relationships between inertial and blade-oriented coordinate systems must be considered for rotorcraft applications. Let $\mathbf{r}_0(t)$, $\mathbf{v}_0(t)$,and $\boldsymbol{\Omega}(t)$ be the position vector of the origin, velocity, and angular velocity of the non-inertial coordinate system relative to the inertial frame, respectively. Then $\mathbf{v}$ can be written as

$$\mathbf{v} = \mathbf{v}_r + \mathbf{v}_c \tag{3}$$

where

$$\mathbf{v}_r = \mathbf{v}_0(t) + \boldsymbol{\Omega}(t) \times [\mathbf{r} - \mathbf{r}_0(t)] \tag{4}$$

and $\mathbf{v}_c(t)$ is the surface element velocity relative to the non-inertial frame, such as blade flapping, lead-lag motion, etc. In the present calculation, $\mathbf{r}_0(t)$ is set to be zero. Also $\mathbf{v}_0(t)$ is zero by setting forward flight velocity at far field. Furthermore, velocity $\mathbf{v}_c$ is set to be zero under the assumption that no solution adaptive grid is used. The set of conservative variables U, such as density, momentum per unit volume, and total internal energy per unit volume is given by the column *vector*

$$U = \begin{bmatrix} \rho \\ \mathbf{m} \\ e \end{bmatrix} \tag{5}$$

One can then define the normal flux component $F_n = \mathbf{n} \cdot \mathbf{F}$, the normal velocity components $u_n = \mathbf{n} \cdot \mathbf{u}$ and $v_n = \mathbf{n} \cdot \mathbf{v} = \mathbf{\Omega}(t) \cdot (\mathbf{r} \times \mathbf{n})$, and the normal relative velocity component $u' = \mathbf{n} \cdot (\mathbf{u} - \mathbf{v}) = u_n - v_n$. The term of $\mathbf{r} \times \mathbf{n}$ is not a function of time and is fixed at each cell for rigid-body rotation. For inviscid flow, the set of variables F_n is given by the column *vector*

$$F_n = \begin{bmatrix} M \\ \mathbf{P} \\ E \end{bmatrix} = \begin{bmatrix} \rho u' \\ \mathbf{m}u' + p\mathbf{n} \\ eu' + pu_n \end{bmatrix} \tag{6}$$

where M, $\mathbf{P}$, and E are the normal flux of mass, momentum, and energy, and p is the pressure. The surface normal unit vector $\mathbf{n}$ can be obtained by

$$\mathbf{n} = \mathbf{C}(\omega t)\mathbf{n}_r \tag{7a}$$

with the rotation matrix

$$\mathbf{C}(\omega t) = \begin{bmatrix} cos(\omega t) & -sin(\omega t) & 0 \\ sin(\omega t) & cos(\omega t) & 0 \\ 0 & 0 & 1 \end{bmatrix} \tag{7b}$$

where $\mathbf{n}_r$ is the cell surface vector represented with respect to the rotation frame and is only calculated once. With the rotation matrix(7b), one need not recalculate coordinates (x, y, z) of the grid points at each time step. The details of the evaluation of $\mathbf{n}_r$ and other grid quantities can be found in Ref. 2.

In the present work, the Euler equations are written using the absolute variables in the inertial frame (that is Eqs. (5)-(6)) for generality. It may be mentioned, however, that the formulation can be easily transformed to the rotational frame by using the rotation matrix

$$C = \begin{bmatrix} 1 & 0 & 0 \\ 0 & \mathbf{C} & 0 \\ 0 & 0 & 1 \end{bmatrix} \tag{8}$$

then one can write

$$U = CU^*, \quad F_n = CF_n^* \tag{9}$$

and a source term $C^T \cdot \dot{C}U^*$ can be derived from the time differentiation. U^* is the vector of so-called absolute variables written in the rotational frame.[3-4] F_n^* can be expressed as

$$F_n^* = \begin{bmatrix} \rho u' \\ \mathbf{C}^T(\mathbf{m}u' + p\mathbf{n}) \\ eu' + pu_n \end{bmatrix} \tag{10}$$

For the hovering case with this transformation, U^* is not a function of time, and therefore an acceleration scheme may be adopted to solve this form of governing equation(Eq.(10) plus source terms). However for the forward flight, this benefit is lost. Furthermore, some care must be taken in order to reproduce uniform flow when using this formula.[2] For these reasons, the inertial formulation was considered preferable for this paper.

4. NUMERICAL ALGORITHM

Several Euler codes for rotors have been developed.[4-10] Most of them use central difference operators with user adjustable dissipation coefficients. The present code uses Steger-Warming flux vector splitting[11] in the circumferential, (or primary flow) direction and Jameson's dissipative terms[12] in the other two directions. The use of flux splitting can avoid the "tuning" of explicit dissipation coefficients. Furthermore the linear stability analysis shows that the use of flux vector splitting combined with upwind differencing in the main flow direction, and central differencing in the other two directions, can result in an unconditionally stable two-factored algorithm.[13]

In the present approach, the conservation law is applied to cells defined by the primary grid.[2] The van Leer MUSCL(monotone upstream-centered scheme for the conservation laws) approach is used to evaluate the conservative variables U^- or U^+ at cell surface.[14-16] They are given by

$$U^-_{j+1/2,k,l} = U_{j,k,l} + \phi_j^-(U_{j,k,l} - U_{j-1,k,l})/2 \tag{11a}$$

$$U^+_{j+1/2,k,l} = U_{j+1,k,l} - \phi_j^+(U_{j+2,k,l} - U_{j+1,k,l})/2 \tag{11b}$$

where first- or second-order approximations are obtained by setting $\phi = 0$ or ϕ =1, respectively. The geometric quantities related to $F^{\xi}_{j+1/2,k,l}$ are evaluated at $j + 1/2, k, l$. The resultant two-factor, flux-splitting algorithm can be summarized by

$$(V + \Delta t\mathcal{L}^+)(V + \Delta t\mathcal{L}^-)\Delta U^n = RHS \tag{12a}$$

$$\mathcal{L}^+ = \delta_\xi^- A^+ + \delta_\varsigma^c C - D_i|_\varsigma \tag{12b}$$

$$\mathcal{L}^- = \delta_\xi^+ A^- + \delta_\eta^c B - D_i|_\eta \tag{12c}$$

$$RHS = -V\Delta t(\delta_\xi^-(\hat{E}^+)^n + \delta_\xi^+(\hat{E}^-)^n + \delta_\eta^c\hat{F}^n + \delta_\varsigma^c\hat{G}^n - D_eU + \frac{U^n\Delta V}{\Delta t}) \tag{12d}$$

$$\delta_\xi^{\mp}A^{\pm}\Delta U = A^{\pm}_{j+1/2,k,l}\Delta U^{\mp}_{j+1/2,k,l} - A^{\pm}_{j-1/2,k,l}\Delta U^{\mp}_{j-1/2,k,l}$$

where the quantities D_i, D_e are the smoothing terms in the crossflow direction,[13] $\hat{E}^{\pm} = \hat{E}^{\pm}(U^{\mp})$, $A^{\pm} = A^{\pm}(U^{\mp})$ and ΔU^- and ΔU^+ are obtained by

$$\Delta U^-_{j+1/2,k,l} = \Delta U_{j,k,l} + \phi_j^-(\Delta U_{j,k,l} - \Delta U_{j-1,k,l})/2 \tag{12e}$$

$$\Delta U^{+}_{j+1/2,k,l} = \Delta U_{j+1,k,l} - \phi^{+}_{j}(\Delta U_{j+2,k,l} - \Delta U_{j+1,k,l})/2 \tag{12f}$$

In Eq. (12), the superscript n is the number of the time steps.

5. BOUNDARY CONDITIONS

For inviscid flow, no flow across the wall boundary is implemented by imposing $u_n = v_n$ on the solid wall. The normal flux component F_n for the wall cell surface becomes

$$F_n = \begin{bmatrix} M \\ \mathbf{P} \\ E \end{bmatrix} = \begin{bmatrix} 0 \\ p\mathbf{n} \\ pv_n \end{bmatrix} \tag{13}$$

The only unknown is pressure, which can be determined by solving the normal momentum equation (total enthalpy is not constant). The normal momentum equation on the wall can be written as

$$-\rho(\mathbf{u}_1 - \mathbf{v}_1).\frac{D\mathbf{n}_1}{Dt} + \rho\mathbf{n}_1.\frac{D\mathbf{v}_1}{Dt} = -p_n \tag{14a}$$

The velocity components required for the normal momentum equation on the wall are determined by

$$\mathbf{u}_1 \cdot t_\xi = (2\mathbf{u}_2 - \mathbf{u}_3) \cdot t_\xi \tag{14b}$$

$$\mathbf{u}_1 \cdot t_\eta = (2\mathbf{u}_2 - \mathbf{u}_3) \cdot t_\eta \tag{14c}$$

and

$$\mathbf{v}_1 \cdot \mathbf{n}_1 = \mathbf{u}_1 \cdot \mathbf{n}_1 \tag{14d}$$

t_ξ and t_η are the vectors joining opposite edge midpoints of cells on the blade surface, which are normal to the surface vector $\mathbf{n}_1$. The subscript 1 represents the blade surface, and 2 or 3 are one or two points away from the blade, respectively.

For the hovering cases, the periodicity is the physical boundary condition and can be implemented at the grid cuts as

$$\rho_1 = \rho_{jmax}, \quad e_1 = e_{jmax}$$

$$\mathbf{u}_{jmax} = \mathbf{C}(-2\pi/n)\mathbf{u}_1 \tag{15}$$

where n is the number of blades and subscripts 1 and $jmax$ refer to ξ direction. There is no additional interpolation required to obtain flow variables at the grid cut because the grid set for each blade is generated to satisfy the periodic condition. For the far field, nonreflection boundary conditions are used.[12] For the inboard of the blades, no flux is allowed through the inboard cylinder.

6. NUMERICAL RESULTS AND VERIFICATION

The first test case is a NACA-0012 infinite aspect ratio wing. A very coarse C-H type grid is used. There are 49 points in the chordwise direction, 5 points in the spanwise direction, and 10 points in the normal-to-the-blade direction. The flow is calculated in both the wing-fixed and inertial coordinate system. The far

field conditions were either set to $M_\infty = 0.8, \alpha = 0°$, or allowed to remain quiescent while moving the body-fitted grid at the same Mach number in the negative x direction. The pressure contours around the wing surface show excellent agreement between these two approaches(Fig.3), though the Mach contours are different by a linear transformation as we should expect(Figs. 4(a)-4(b)). Furthermore, the instantaneous streamline pattern shows the doublet characteristic of this wing in rectilinear motion(Fig. 5)

The second case is a nonlifting two-blade rotor in hover, which has been investigated experimentally by Caradonna and Tung.[17] In this and succeeding cases, the equations are solved in the inertial frame. The blade is an untwisted, untapered blade with a constant NACA-0012 profile and an aspect ratio of 6. The flow condition is $M_T = 0.52$. The pressure comparison is quite good at various locations as shown in Fig. 6. This solution was computed using periodic boundary conditions (that is $n = 2$ in Eq. (15)).

The third case is a six-blade rotor in hover. The relative Mach number contours are shown in Figs. 7(a)-(b)(Color Plate *I*) for $M_T = 0.85$ and 0.9. The sonic line is represented by the white line in this and succeeding figures. Also, the violet color represents supersonic flow with respect to a non-inertial coordinate system. The different physical characteristics are observed in the tip region. When the tip Mach number is increased, the supersonic region on the blade is delocalized and connects with the supersonic far field. This effect was also observed in the experiment for the same range of Mach number.[18]

The fourth case is a study of the effects of different numbers of blades. For comparison of the nonlifting 2-blade and 6-blade rotor, the grid density is essentially the same in both cases. The low pressure peak is found to be diminished slightly, and the delocalization phenomenon is also slightly delayed by increasing the number of blades as shown in Fig. 8. To understand this blade-to-blade interference effect, it is useful to consider incompressible flow over parallel infinite cylinders. The distance between each neighbor cylinder is b. By taking leading terms, the complex potential W for the uniform flow over infinite cylinders can be approximated as

$$
\begin{aligned}
W \approx -\frac{\mu}{a^2} z + \sum_{n=1}^{n=N} & \frac{\mu a^2}{b^2(z - x_n - b')} + \frac{\mu a^2}{b^2(z - x_n + b')} \\
& - \frac{\mu' a^2}{(b-b')^2(z - x_n - (b-b')')} - \frac{\mu' a^2}{(b+b')^2(z - x_n - (b+b')')} \\
& - \frac{\mu' a^2}{(b-b')^2(z - x_n + (b-b')')} - \frac{\mu' a^2}{(b+b')^2(z - x_n + (b+b')')} \\
& + \frac{\mu a^2}{(2b)^2(z - x_n - (\frac{a^2}{2b}))} + \frac{\mu a^2}{(2b)^2(z - x_n + (\frac{a^2}{2b}))} \\
& - \frac{\mu}{z - x_n}
\end{aligned}
$$

where $\mu = U_\infty a^2$, and additional quantities are defined as follows,

$$
b' = \frac{a^2}{b}, \quad (b \pm b')' = \frac{a^2}{(b \pm b')}, \quad \mu' = \frac{\mu a^2}{b^2}
$$

In these equations, x_n is the location of the center of each cylinder, a is the radius of a cylinder, n is the number of cylinders and N is a large number. The pressure comparison is shown on Fig. 9. Results are presented for $b = 5$ radii, 10 radii, and ∞. When the cylinders get closer, the peak of pressure becomes lower. That is the same trend as seen in Fig. 8, even though compressibility and three-dimensional effects are additional factors.

The fifth case is a nonlifting forward-flight case, studied experimentally by Caradonna et al.[19] The experiment tested a stiff, two-bladed, untwisted, untapered blade with a constant NACA-0012 profile. The blade was pressure-instrumented at $r/R = 0.893$. Figure 10 compares computed and experimental results for a blade-tip Mach number of 0.8 and an advance ratio μ of 0.2. Here, pressure coefficients are plotted at a single radial location for a variety of rotor azimuthal angles. The grid distributed on each blade half surface contains 61 points in the chordwise direction, 19 points in the spanwise direction, and 46 points normal to the blade. The total number of grid points is about 300,000.

The computational results agree closely with experimental data. The location of the shock for a variety of azimuthal angles is captured very well by the present algorithm. The relative Mach number contours on the rotor disk are shown in Fig. 11 (Color Plate *II*). The blue to red represents the low to high Mach number region. The supersonic region is represented by violet outside the white line. The results show that the shock exists in the advancing side and disappears in the retreating side. The contour plots vary with azimuthal angle, which is different from the results for hovering cases shown in Fig. 7.

7. CONCLUDING REMARKS

A finite-volume, partially flux-vector split Euler code with a cylindrical grid topology for multiblade rotor has been developed. The present results of nonlifting multiblade rotors show that this code and grid topology are potentially very useful for complex multiblade rotor flow. The computed results show good agreement with experimental data in either hover or forward flight. In hovering cases, the delocalization phenomenon is observed. Moreover, the effects of different numbers of blades for the nonlifting multiblade rotor are also examined. When the number of blades is increased, the results indicate that the low-pressure peak is reduced slightly and consequently the delocalization is delayed slightly. In forward-flight cases, the shock can also be captured quite well at a variety of rotor azimuthal angles. The lifting cases will be studied in the near future, along with an extension to rotor-body interactions.

REFERENCES

1. M. M. Rai, *Unsteady Three-Dimensional Navier-Stokes Simulations of Turbine Rotor-Stator Interaction*, AIAA Paper 87-2058, 1987.

2. M. Vinokur, *An Analysis of Finite-Difference and Finite-Volume Formulations of Conservation Laws*, NASA CR-177416, Jun. 1986.

3. D. G. Holmes and S. S. Tong, *A Three-Dimensional Euler Solver for Turbomachinery Blade Rows*, Journal of Engineering for Gas Turbines and Power, Vol. 107, 1985, 258–264.

4. R. K. Agarwal and J. E. Deese, *An Euler Solver for Calculating the Flowfield of a Helicopter Rotor in Hover and Forward Flight*, AIAA Paper 87-1427, Jun. 8-10, 1987.

5. I. C. Chang and C. Tung, *Euler Solution of the Transonic Flow for a Helicopter Rotor*, AIAA Paper 87-0523, Jan. 1987.

6. N. L. Sankar, B. E. Wake and S. G. Lekoudis, *Solution of the Unsteady Euler Equations for Fixed and Rotor Wing Configurations*, J. Aircraft, Vol. 23, 1986, 283–289.

7. T. W. Roberts and E. M. Murman, *Solution for the Flow Around a Hovering Helicopter Rotor*, AIAA Paper 86-1784, Jun. 1986.

8. A. Eberle, *A New Flux Extrapolation Scheme Solving the Euler Equations for Arbitrary 3-D Geometry and Speed*, MBB/LKE122/S/PUB/140, 1984.

9. N. Kroll, *Computation of the Flow Fields of Propellers and Hovering Rotors Using Euler Equations*, Twelfth European Rotorcraft Form, Paper No. 28, 1986.

10. H. Stahl, *Application of a 3D Euler Code to Transonic Blade Tip Flow*, Twelfth European Rotorcraft Form, Paper No. 29, 1986.

11. J. L. Steger and R. F. Warming, *Flux Vector Splitting of the Inviscid Gasdynamic Equations with Application to Finite-Difference Methods*, J. Comp. Phys, Vol. 40, 1981, 263–293.

12. A. Jameson, W. Schmidt and E. Turkel, *Numerical Solutions of the Euler Equations by Finite Volume Methods Using Runge-Kutta Time-Stepping Schemes*, AIAA Paper 81-1259, Jun. 1981.

13. S. X. Ying, *Three-Dimensional Implicit Approximately Factored Schemes for the Equations of Gasdynamics*, PhD Thesis, Department of Aeronautics and Astronautics, Stanford University, Jun. 1986.

14. W. K. Anderson, J. L. Thomas and B. Van Leer, *Comparison of Finite Volume Flux Vector Splittings for the Euler Equations*, AIAA J., Vol. 24, Sep. 1986.

15. B. van Leer, *Towards the Ultimate Conservative Difference Scheme. V. A Second-Order Sequel to Godunov's Method*, Journal of Computational Physics, Vol. 32, 1979, 101-136.

16. B. van Leer, *On the Relation Between the Upwind-Difference Schemes of Godunov, Engquist-Osher, and Roe*, ICASE Report 81-11, 1981.

17. F. X. Caradonna and C. Tung, *Experimental and Analytical Studies of a Model Helicopter Rotor in Hover*, Vertica, Vol. 5, 1981, 149-161.

18. F. H. Schmitz and Y. H. Yu, *Helicopter Impulse Noise: Theoretical and Experimental Status*, Journal of Sound and Vibration, 1986, 361-422.

19. F. X. Caradonna, G. H. Laub and C. Tung, *An Experimental Investigation of the Parallel Blade-Vortex Interaction*, NASA TM-86005, Nov. 1984.

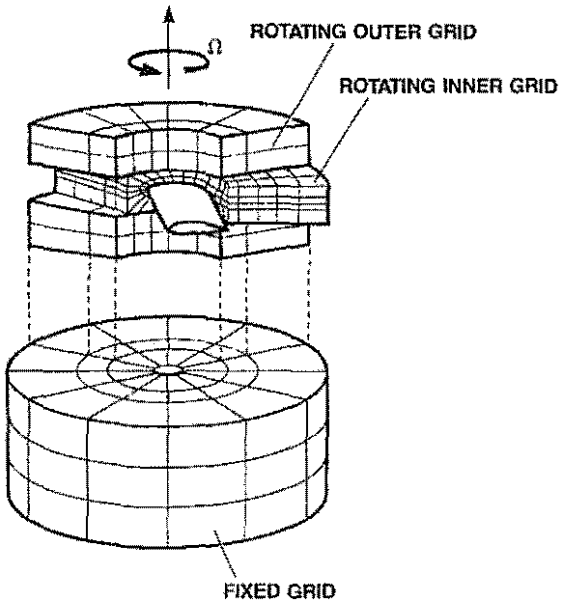

Fig. 1 Cylindrical grid topology for rotor-fuselage interaction.

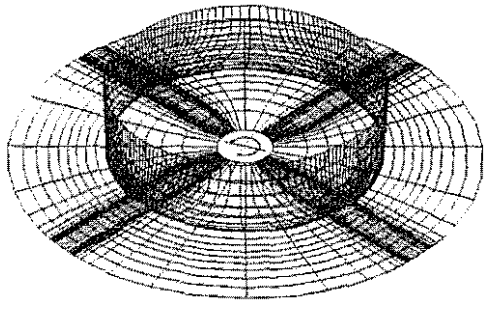

Fig. 2 Cylindrical grid for a four-blade rotor.

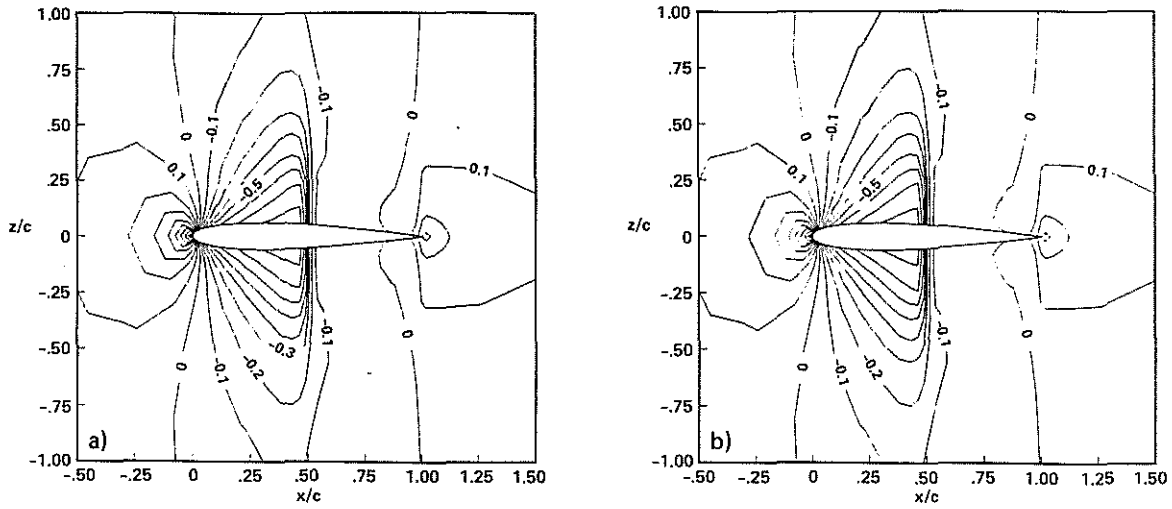

Fig. 3 Comparison of pressure contours for a NACA-0012 airfoil with two different approaches. a) Wing-fixed coordinate system with far field condition $M_\infty = 0.8$ and $\alpha = 0.0°$; b) Inertial coordinate system with moving grid.

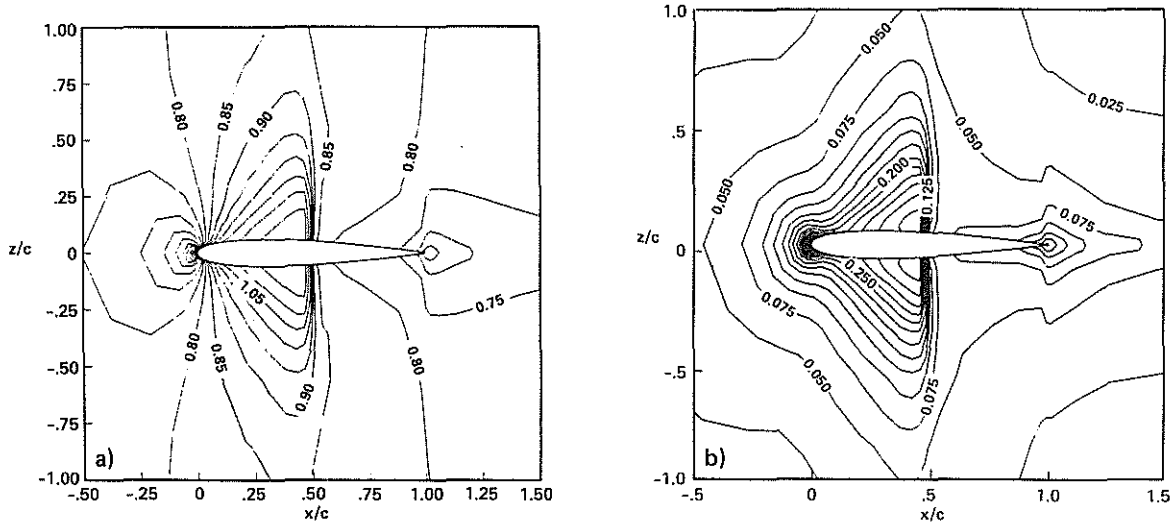

Fig. 4 Comparison of Mach contours for a NACA-0012 airfoil with two different approaches. a) Wing-fixed coordinate system with far field condition $M_\infty = 0.8$ and $\alpha = 0.0°$; b) Inertial coordinate system with moving grid.

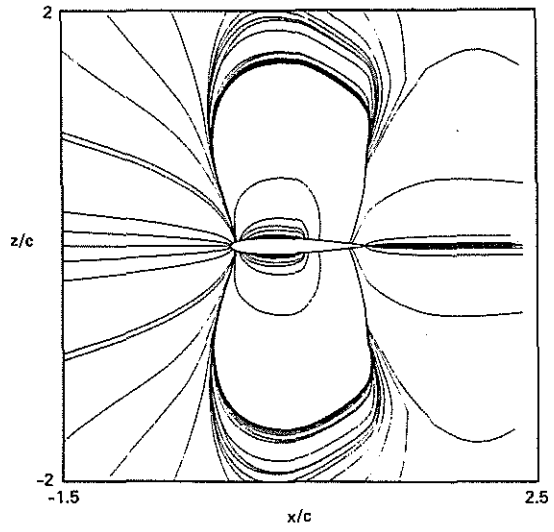

Fig. 5 Instantaneous streamline pattern of a NACA-0012 airfoil in rectilinear motion.

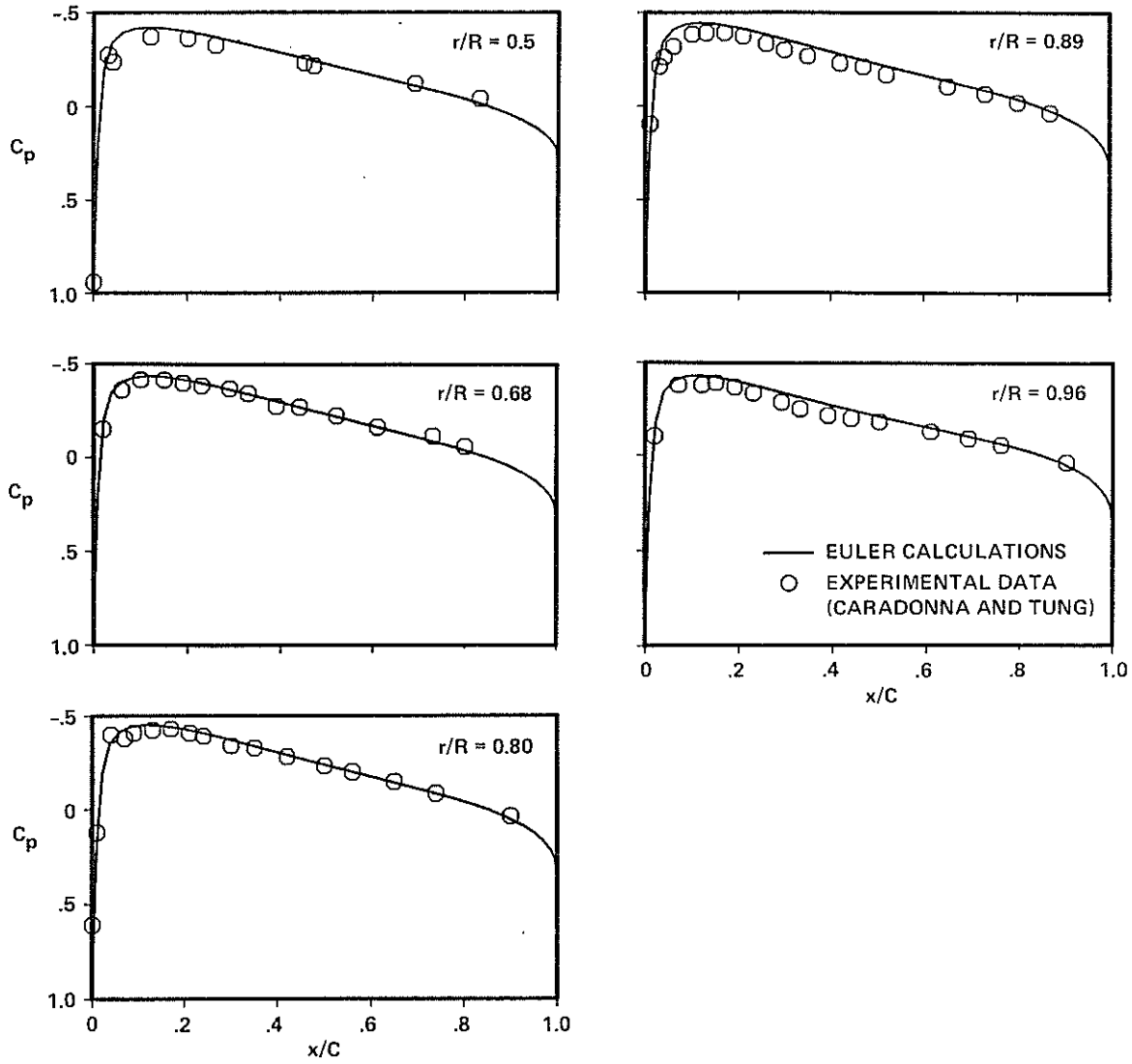

Fig. 6 Surface pressure results at various locations for a hovering two-blade rotor, $M_T = 0.52$, aspect ratio = 6, nonlifting, untwisted, untapered NACA-0012 blade.

Fig. 7 (Color Plate *I*) follows page 2-2-13.

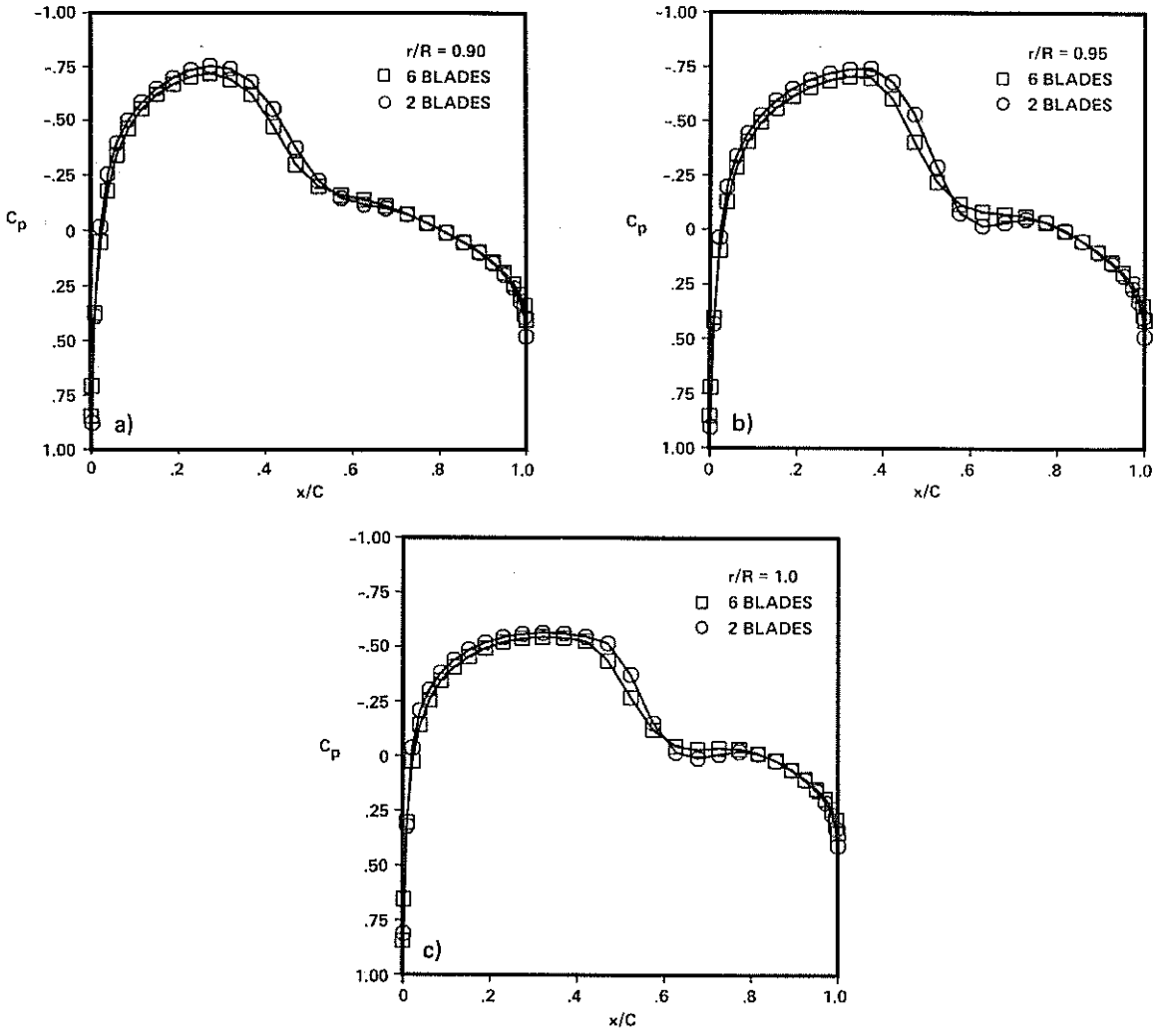

Fig. 8 Comparison of surface pressure results for hovering rotors with different numbers of blades, $M_T = 0.9$, aspect ratio = 6, nonlifting, untwisted, untapered NACA-0012 blade. a) r/R = 0.90; b) r/R = 0.95; c) r/R = 1.0.

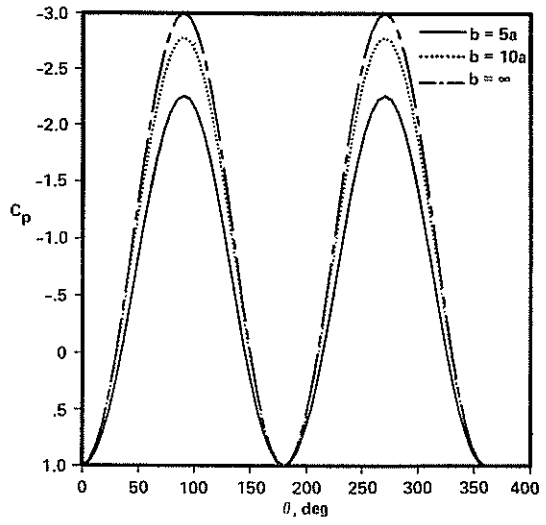

Fig. 9 Comparison of surface pressure results for inviscid incompressible flows over infinite cylinders.

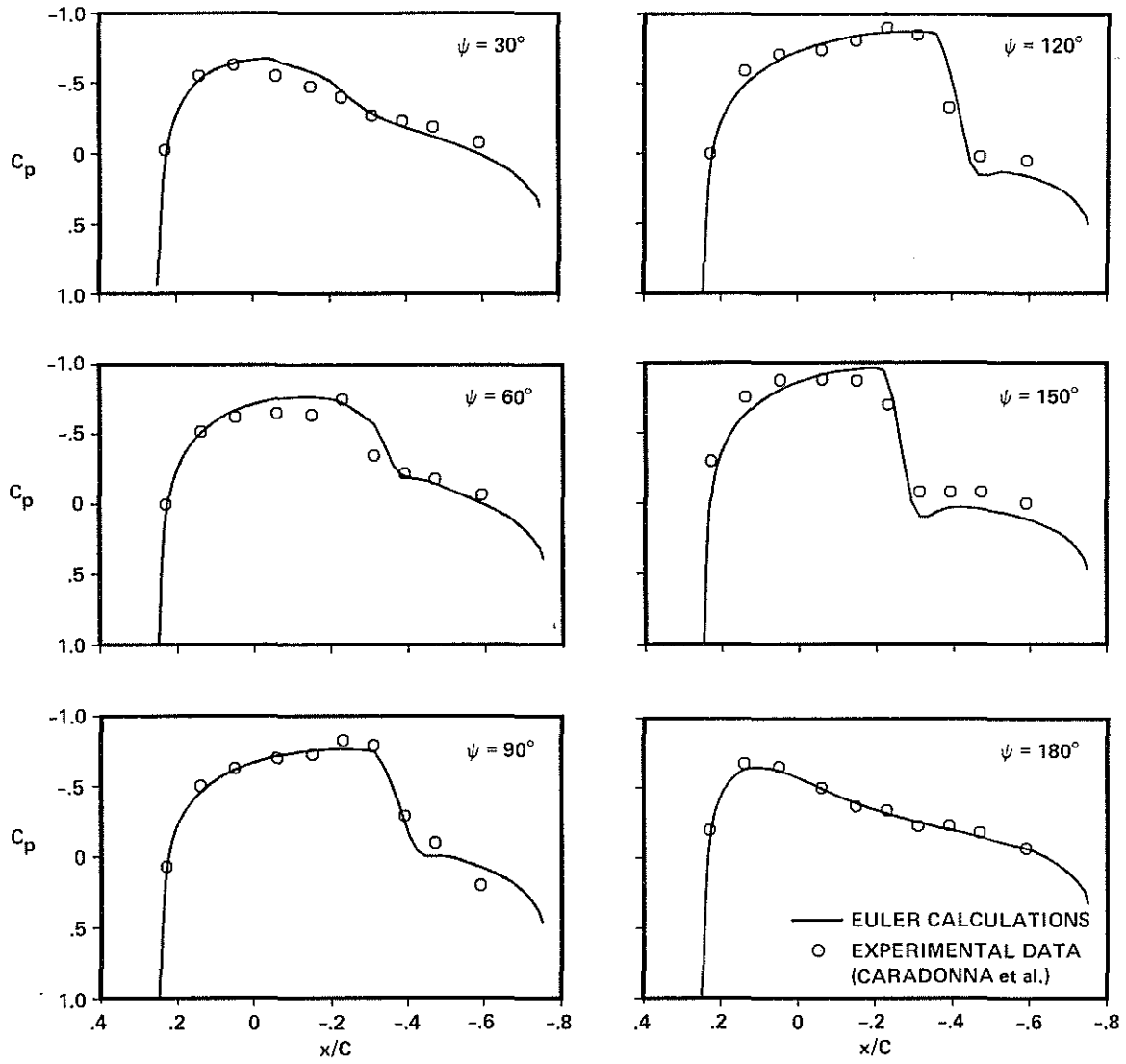

Fig. 10 Surface pressure results at the advancing side for a forward-flight two-blade rotor, $M_T = 0.8, \mu = 0.2$, aspect ratio = 7, nonlifting, untwisted, untapered NACA-0012 blade.

Fig. 11 (Color Plate *II*) follows page 2-2-13.

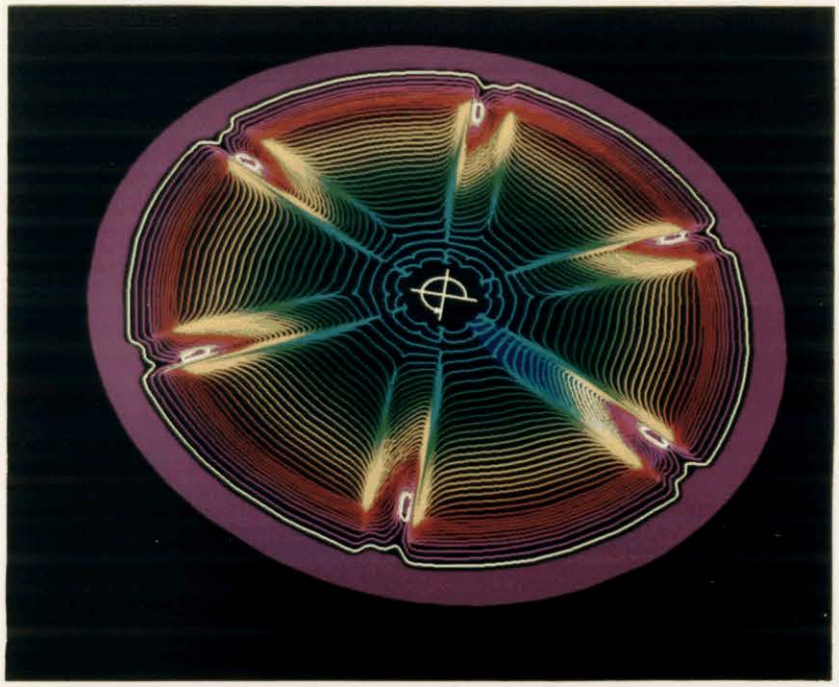

(a)

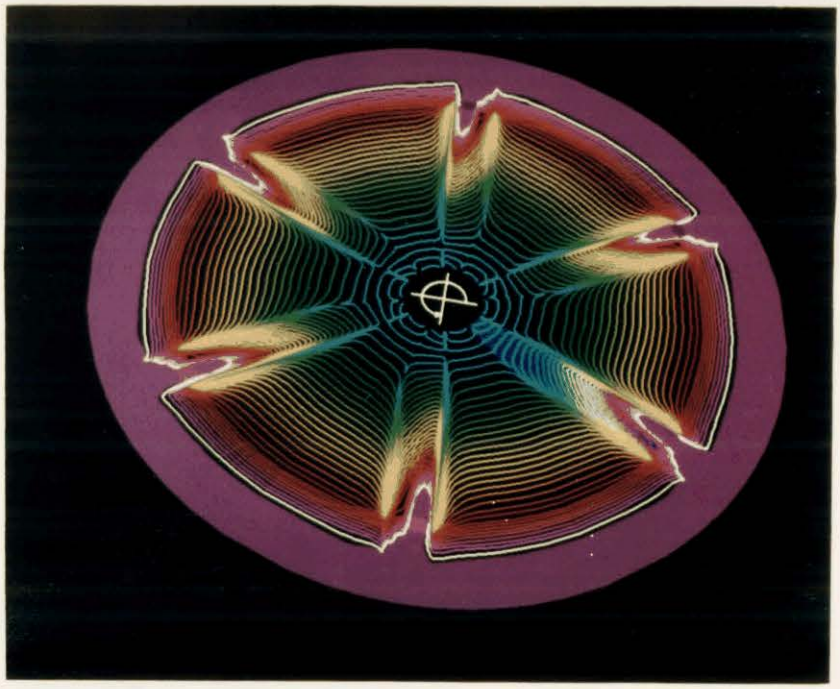

(b)

Fig. 7 Mach contours for a hovering six-blade rotor, aspect ratio = 6, nonlifting, untwisted, untapered NACA-0012 blade. a) M_T = 0.85; b) M_T = 0.9.

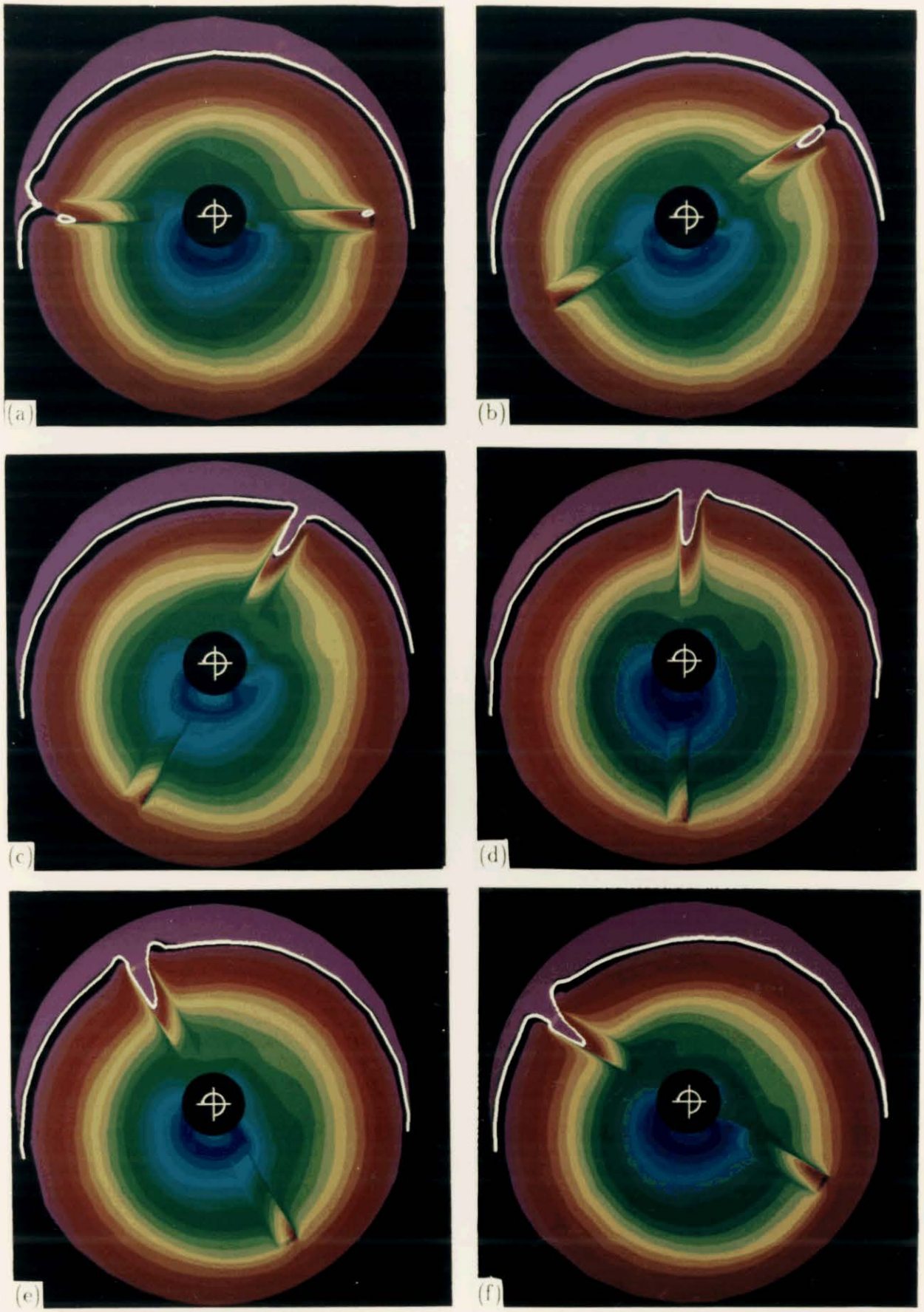

Fig. 11 Mach contours at various azimuthal angles for a forward-flight two-blade rotor, $M_T = 0.8, \mu = 0.2$, aspect ratio = 7, nonlifting, untwisted, untapered NACA-0012 blade. a) $\Psi = 0°$; b) $\Psi = 30°$; c) $\Psi = 60°$; d) $\Psi = 90°$; e) $\Psi = 120°$; f) $\Psi = 150°$.

2-2 Color Plate *II*